



**HAL**  
open science

## Crystal Structure, DFT Calculation, and Hirshfeld Surface Analysis of the 1-(Cyclohex-1-en-1-yl)-3-(prop-2-yn-1-yl)-1,3-dihydro-2H-benzimidazol-2-one

Mohamed Adardour, Marouane Ait Lahcen, Ismail Hdoufane, Mohammed M Alanazi, Mohamed Loughzail, Hénia Mousser, Solenne Fleutot, Michel François, Driss Cherqaoui, Abdesselam Baouid

### ► To cite this version:

Mohamed Adardour, Marouane Ait Lahcen, Ismail Hdoufane, Mohammed M Alanazi, Mohamed Loughzail, et al.. Crystal Structure, DFT Calculation, and Hirshfeld Surface Analysis of the 1-(Cyclohex-1-en-1-yl)-3-(prop-2-yn-1-yl)-1,3-dihydro-2H-benzimidazol-2-one. *Crystals*, 2023, 13 (12), pp.1661. 10.3390/cryst13121661 . hal-04323041

**HAL Id: hal-04323041**

**<https://hal.science/hal-04323041v1>**






Submitted on 5 Dec 2023

**HAL** is a multi-disciplinary open access archive for the deposit and dissemination of scientific research documents, whether they are published or not. The documents may come from teaching and research institutions in France or abroad, or from public or private research centers.

L'archive ouverte pluridisciplinaire **HAL**, est destinée au dépôt et à la diffusion de documents scientifiques de niveau recherche, publiés ou non, émanant des établissements d'enseignement et de recherche français ou étrangers, des laboratoires publics ou privés.

## Article

# Crystal Structure, DFT Calculation, and Hirshfeld Surface Analysis of the 1-(Cyclohex-1-en-1-yl)-3-(prop-2-yn-1-yl)-1,3-dihydro-2H-benzimidazol-2-one

Mohamed Adardour <sup>1</sup>, Marouane Ait Lahcen <sup>1</sup>, Ismail Hdoufane <sup>1,\*</sup>, Mohammed M. Alanazi <sup>2</sup>, Mohamed Loughzail <sup>1</sup>, Hénia Mousser <sup>3</sup>, Solenne Fleutot <sup>4</sup>, Michel François <sup>4</sup>, Driss Cherqaoui <sup>1,5</sup> and Abdesselam Baouid <sup>1</sup>

- <sup>1</sup> Laboratory of Molecular Chemistry, Faculty of Sciences Semlalia, BP 2390, Cadi Ayyad University, Marrakech 40000, Morocco; mohamed.adardour@ced.uca.ac.ma (M.A.); m.aitlahcen@ced.uca.ac.ma (M.A.L.); loughzail@gmail.com (M.L.); cherqaoui@uca.ma (D.C.); baouid@uca.ac.ma (A.B.)
- <sup>2</sup> Department of Pharmaceutical Chemistry, College of Pharmacy, King Saud University, P.O. Box 2457, Riyadh 11451, Saudi Arabia; mmalanazi@ksu.edu.sa
- <sup>3</sup> Laboratoire de Physicochimie Analytique et Cristallographie de Matériaux, Organométalliques et Biomoléculaires, Université des Frères Mentouri, Constantine 1, Constantine 25000, Algeria; bouzidi.henia@yahoo.fr
- <sup>4</sup> Institut Jean Lamour, Université de Lorraine, CNRS, IJL, F-54000 Nancy, France; solenne.fleutot@univ-lorraine.fr (S.F.); michel.francois@univ-lorraine.fr (M.F.)
- <sup>5</sup> Sustainable Materials Research Center (SUSMAT-RC), Mohammed VI Polytechnic University, Benguerir 43150, Morocco
- \* Correspondence: i.hdoufane@uca.ac.ma



**Citation:** Adardour, M.; Ait Lahcen, M.; Hdoufane, I.; Alanazi, M.M.; Loughzail, M.; Mousser, H.; Fleutot, S.; François, M.; Cherqaoui, D.; Baouid, A. Crystal Structure, DFT Calculation, and Hirshfeld Surface Analysis of the 1-(Cyclohex-1-en-1-yl)-3-(prop-2-yn-1-yl)-1,3-dihydro-2H-benzimidazol-2-one. *Crystals* **2023**, *13*, 1661. <https://doi.org/10.3390/cryst13121661>

Academic Editors: Danny A Rehn, Ann E. Mattsson, Roxanne Tutcheon, Jian-Xin Zhu and Christopher Lane

Received: 2 November 2023

Revised: 23 November 2023

Accepted: 30 November 2023

Published: 3 December 2023



**Copyright:** © 2023 by the authors. Licensee MDPI, Basel, Switzerland. This article is an open access article distributed under the terms and conditions of the Creative Commons Attribution (CC BY) license (<https://creativecommons.org/licenses/by/4.0/>).

**Abstract:** In this paper, we describe the synthesis and structural characterization of the 1-(cyclohex-1-en-1-yl)-3-(prop-2-yn-1-yl)-1,3-dihydro-2H-benzimidazol-2-one (**2**) via IR, NMR (<sup>1</sup>H and <sup>13</sup>C), and HRMS. The crystal structure of the isolated organic compound **2** was confirmed through single-crystal X-ray diffraction analysis. The experimental results regarding the molecular geometry and intermolecular interactions within the crystal are in accordance with the DFT calculations and Hirshfeld surface analysis.

**Keywords:** benzimidazolone derivative; cyclohexenyl; X-ray diffraction; DFT; Hirshfeld surface

## 1. Introduction

Aromatic compounds with heterocyclic structures incorporating nitrogen and oxygen play an important role in organic chemistry synthesis. Benzimidazoles containing nitrogen are well known for their wide range of biological activities [1–4]. In addition, they have been studied extensively for their anticancer activity [5], antifungal agents [1,6], antiviral activity [7,8], and antidiabetic properties [9,10]. Moreover, the benzimidazolone nucleus is often used as a scaffold for the development of therapeutic molecules with medicinal and biological applications. Benzimidazolone derivatives display noticeable pharmacological applications such as antimicrobial [11,12], anti-inflammatory [13], and antitumor agents [7,14]. Additionally, the use of benzimidazole and its derivatives as corrosion inhibitors for mild steel in an acidic medium has been reported [15,16]. Several methodologies can be employed for the synthesis of benzimidazolone derivatives, with one common approach involving the condensation reaction between *o*-phenylenediamine and ketoester derivatives [17,18].

Within the various categories of heterocycles, benzimidazole derivatives have gained notable recognition in medicinal chemistry [19–21]. As a result, significant interest has been directed toward the creation of new benzimidazole systems. Since the N-alkylation of benzimidazole derivatives generates rigid analogs, it is highly desirable to develop such

scaffolds [22–24]. Recently, alkylating agents have been extensively studied, which has led to the development of many biologically active benzimidazole compounds, particularly molecules that are based on a triazolic moiety [25,26]. Figure 1 shows some different compounds reported in the literature that have been prepared for their biological activities from benzimidazole and its derivatives.

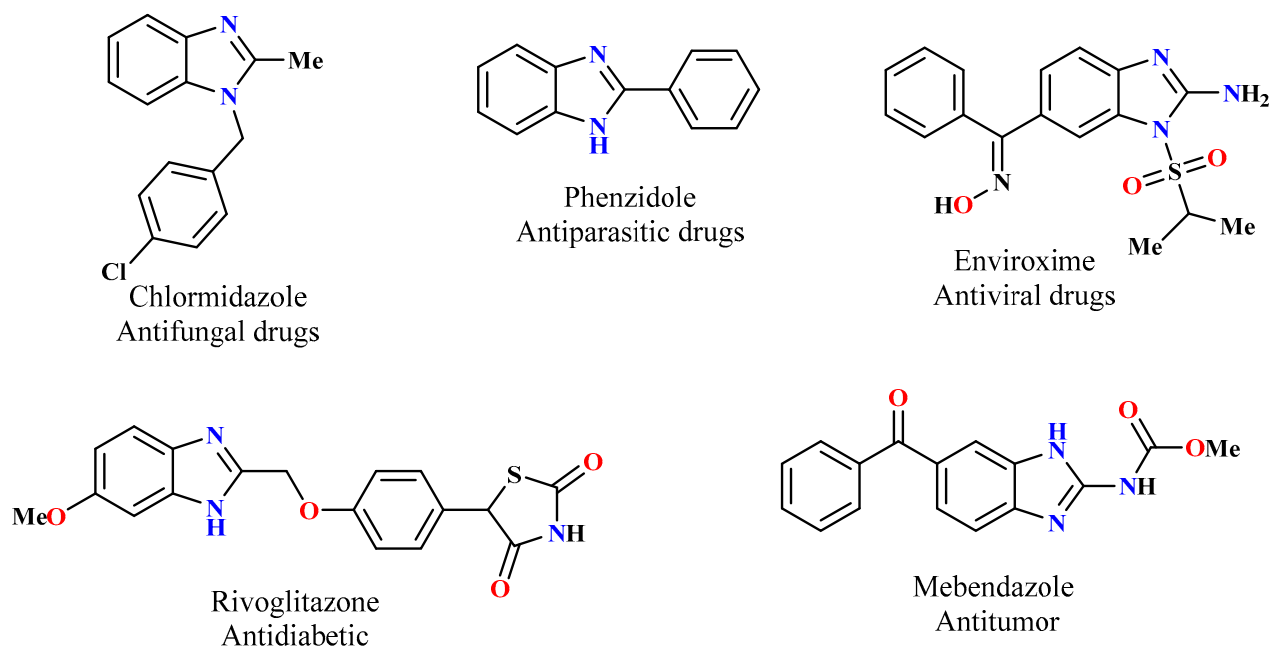


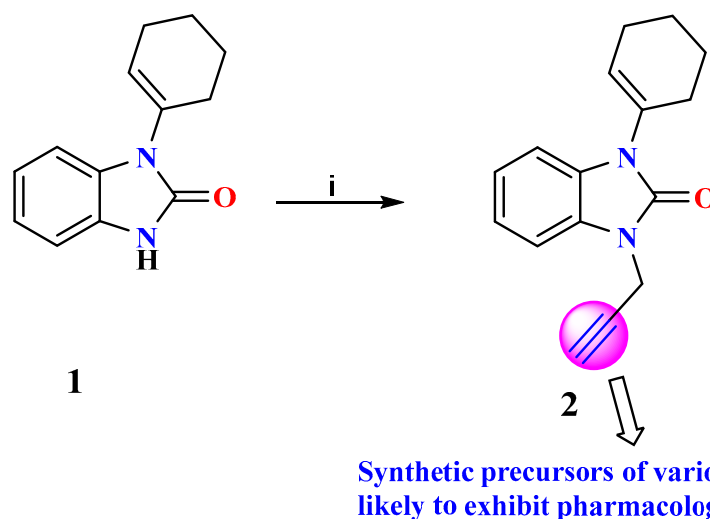
**Figure 1.** Examples of biologically active benzimidazole derivatives.

In this work, we approached the synthesis of benzoimidazol-2-one **2** through the solid–liquid phase-transfer alkylation of benzimidazolone **1**. The structure of (**2**) was established using FT-IR and NMR methods and confirmed through a single-crystal X-ray structure determination. Furthermore, Hirshfeld surface (HS) analysis was used to reveal the different intramolecular contacts, their percentage contribution, the contour and surface plots ( $d_{\text{norm}}$ ,  $d_i$ , and  $d_e$ ), and the major as well as minor contributions of the contacts for compound **2**. Furthermore, the chemical activity parameters determined via the molecular electrostatic potential (MEP) were investigated, demonstrating the nucleophilic and electrophilic character, which is related to the charge distribution around the crystal molecule (**2**).

## 2. Results and Discussion

### 2.1. Synthesis and Structural Characterization

The condensation reaction, a valuable synthetic process in organic chemistry, leads to the formation of benzimidazole and benzodiazepine derivatives. Continuing our previous investigations on the synthesis of benzimidazolone derivatives, we report the synthesis of 1-(cyclohex-1-en-1-yl)-3-(prop-2-yn-1-yl)-1,3-dihydro-2H-benzimidazol-2-one (**2**) in one step using a direct alkylation reaction under phase-transfer catalysis conditions (Scheme 1). The title compound (**2**) was synthesized through the direct *N*-alkylation of benzimidazolone **1** using a previously described process [18,22]. Compound **1** was reacted with propargyl bromide which acted as a catalyst. The reaction was carried out at room temperature for 6 h. Then, the reaction mixture was purified with a hexane/ethyl acetate mixture as an eluent, and then we filtered off the precipitated solid, dried well, and recrystallized from ethyl acetate to prepare **2** with a good yield.



**Scheme 1.** Reagent and condition: (i) R-X,  $K_2CO_3$  and DMF/ $CH_3CN$ , T.A, 6 h.

The structure of **2** was determined using FT-IR and NMR spectroscopy methods, with extensive validation accomplished by cross-referencing the acquired spectroscopic data with the available literature [18]. Furthermore, the geometric arrangement of the chemical was validated using XRD analysis, providing additional confirmation of its structural characteristics.

## 2.2. FT-IR Analysis

The infrared (IR) spectrum of **2** (KBr pellet,  $cm^{-1}$ ) reveals prominent characteristic peaks, as illustrated in Figure 2. Specifically, the  $CH_2$  group exhibits a notable peak at  $2930\text{ cm}^{-1}$ , the C–N stretch appears at  $1404\text{ cm}^{-1}$ , while other distinctive groups, such as the C=O stretch and the C≡C triple bond, are observed at  $1710\text{ cm}^{-1}$  and  $2125\text{ cm}^{-1}$ , respectively. For a more comprehensive understanding, the theoretical IR spectrum was computed using the B3LYP/6-311++G(d,p) level in the gas phase and is presented in Figure 2. The most important experimental and calculated harmonic stretching frequencies are listed in Table 1. Comparing the values, it is evident that the theoretical FT-IR, derived from the same basis-set calculations, generally aligns well with the experimental data, as summarized in Table 1.

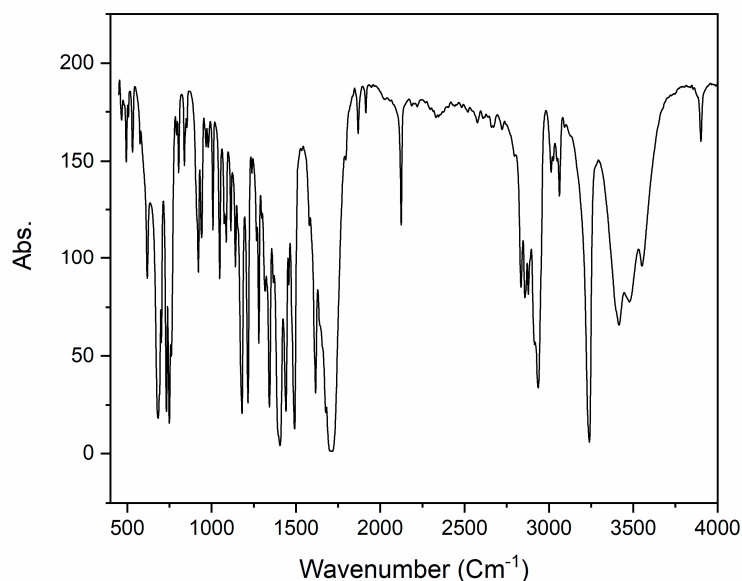


**Figure 2.** Experimental IR spectrum of compound **2**.

**Table 1.** Vibrational study of compound **2** ( $\text{cm}^{-1}$ ).

Assignments	Experimental	B3LYP/6-311++G(d,p)
$\nu_{\text{CH}_2}$	2930	3022
$\nu_{\text{C-N}}$	1404	1411
$\nu_{\text{C=O}}$	1710	1771
$\nu_{\text{C}\equiv\text{C}}$	2125	2223
$\nu_{\text{C=C}}$ (Aromatic)	1620	1648

### 2.3. X-ray Diffraction and Geometry Optimization

The molecular structure of **2** is depicted in Figure 3a. The benzimidazole unit (N1/C1/N2/C2-C7) is almost planar, with maximum deviations of  $-0.012$  (1) Å for atom N1. The cyclohexenyl ring is disordered over two conformations and both it and the  $\text{NCH}_2\text{C}\equiv\text{CH}$  group are rotated out of the mean benzimidazole plane. The benzimidazole plane makes dihedral angles of  $119.26^\circ$  and  $111.72^\circ$  with the base of the cyclohexenyl ring (N1-C8-C9) and the approximately planar (N2-C14-C15) propynyl chain, respectively. The dihedral angle between the cyclohexenyl ring and the  $\text{NCH}_2\text{C}\equiv\text{CH}$  group is  $58.99^\circ$ . The major conformation of the cyclohexenyl ring has a half-chair conformation with puckering parameters of  $Q = 0.496(2)$  Å,  $\theta = 128.1(2)$ , and  $\varphi = 23.4$  (4) $^\circ$  [27].

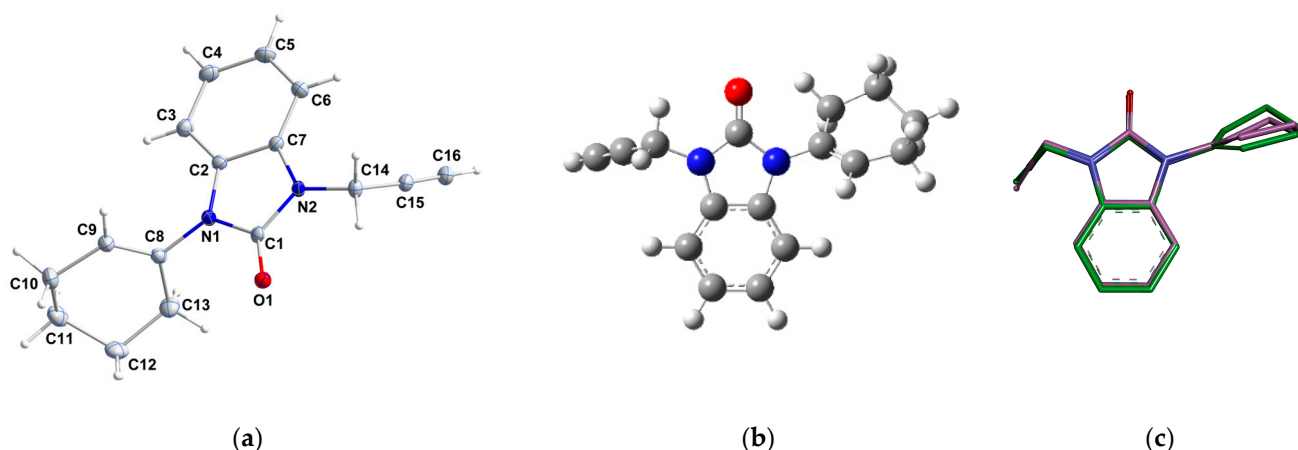


**Figure 3.** (a) ORTEP of compound **2** at a 50% probability level (only the major disorder component is shown), (b) optimized structure of compound **2**, and (c) superimposition of the X-ray structure (green) and the optimized structure (magenta) on the studied molecule **2**.

Table 2 provides a summary of the crystal data, the data collection process, and details of the structural refinement. The positioning of C-bound H atoms was determined through calculated positions, where C-H distances ranged from 0.93 to 0.97 Å. Subsequently, refinement was conducted using the riding-model approximation, with  $\text{Uiso}(\text{H}) = 1.2\text{--}1.5$  Ueq of the respective parent atom, as depicted in Table 3.

**Table 2.** Details of the XRD data collection and structure refinement parameters for **2**.

Empirical Formula	$\text{C}_{16}\text{H}_{16}\text{N}_2\text{O}$
Crystal system	Monoclinic,
Space group	$P2_1/c$
Temperature (K)	293 (2)
$a, b, c$ (Å)	11.591 (5), 14.988 (5), 7.570 (5)
$\beta$ ( $^\circ$ )	92.134 (5)
$V$ (Å <sup>3</sup> )	1314.2 (11)
$Z$	4
$\mu$ ( $\text{mm}^{-1}$ )	0.081
Crystal size (mm)	$0.2 \times 0.1 \times 0.1$

Table 2. Cont.

Empirical Formula	C <sub>16</sub> H <sub>16</sub> N <sub>2</sub> O
Absorption coefficient	0.081 mm <sup>-1</sup>
No. of measured, independent, and observed [ $I > 2\sigma(I)$ ] reflections	31,171, 4013, 3287
R <sub>int</sub>	0.0403
( $\sin \theta / \lambda$ ) <sub>max</sub> (Å <sup>-1</sup> )	0.001
$R[F^2 > 2\sigma(F^2)]$ , $wR(F^2)$ , S	0.04554, 0.1264, 1.056
No. of reflections	4013
No. of parameters	185
Largest diff. peak and hole (e Å <sup>-3</sup> )	0.440, -0.324

Table 3. Hydrogen bond geometry (Å, °).

D-H...A	D-H	H...A	D...A	Angle
C5-H5...Cg2 <sup>a,i</sup>	0.93	2.93	3.746(3)	147
C12-H12B...Cg2 <sup>a,ii</sup>	0.97	2.78	3.576(8)	140
C14-H14B...O <sup>iii</sup>	0.97	2.54	3.2299(18)	127.9
C16-H16...O1 <sup>i</sup>	0.93	2.39	3.203(3)	146

<sup>a</sup> Cg2 is the centroid of the C2-C7 benzene ring. Symmetry code: <sup>(i)</sup>  $-x, -y + 1/2, z + 1/2$ ; <sup>(ii)</sup>  $x, y, z - 1$ ; <sup>(iii)</sup>  $-x + 1, -y + 1, -z + 2$ .

In the crystal, C14-H14B...O1 and C16-H16...O1 hydrogen bonds plus C5-H5...Cg2 and C12-H12B...Cg2 interactions (Table 3) form layers of molecules parallel to the *bc* plane (Figure 4), which stack along the *a*-axis direction with normal van der Waals contacts (Figure 5).

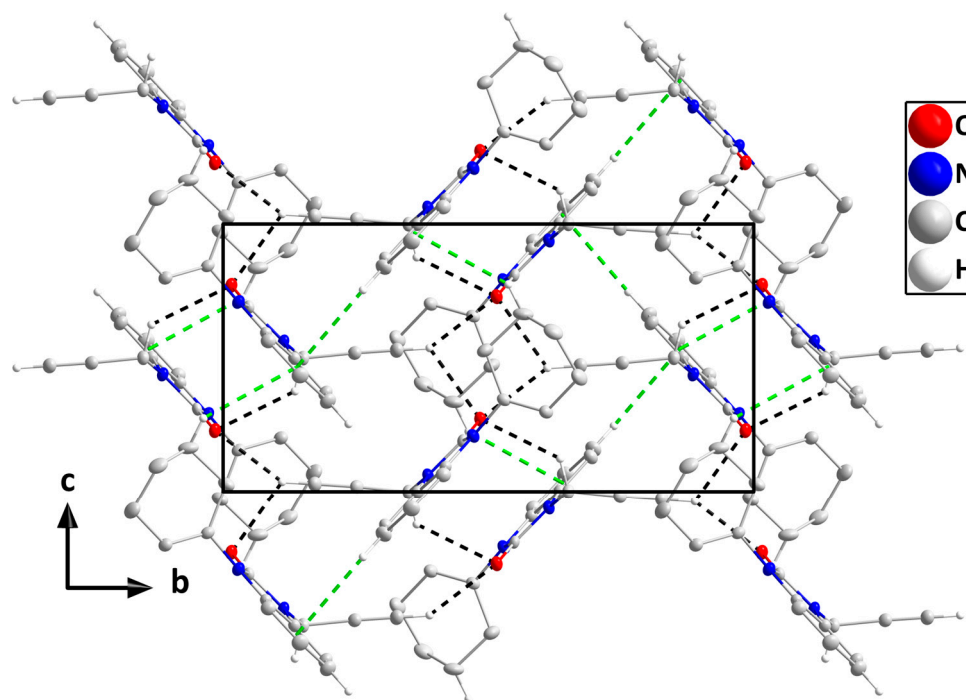
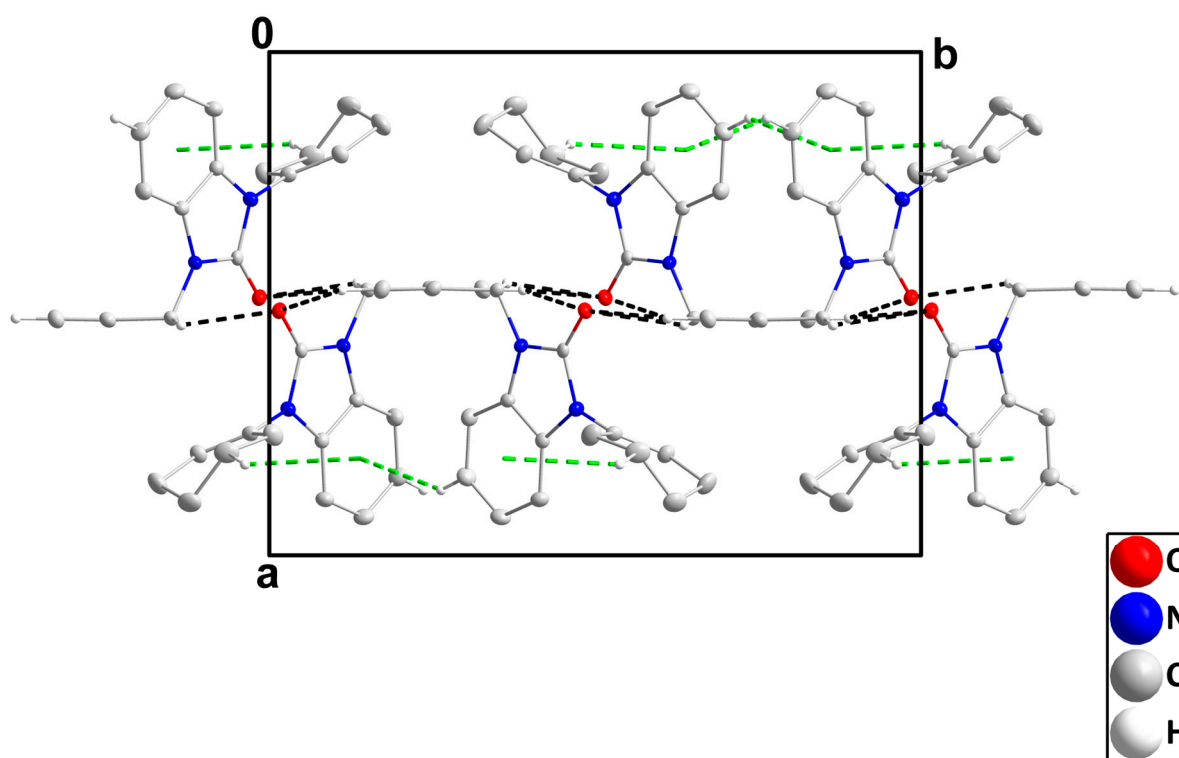


Figure 4. A portion of one layer, observed along the *a*-axis orientation, illustrates C-H...O hydrogen bonds and C-H... $\pi$ (ring) interactions denoted by black and green dashed lines, respectively. For clarity, hydrogen atoms with no interaction are omitted from the representation.



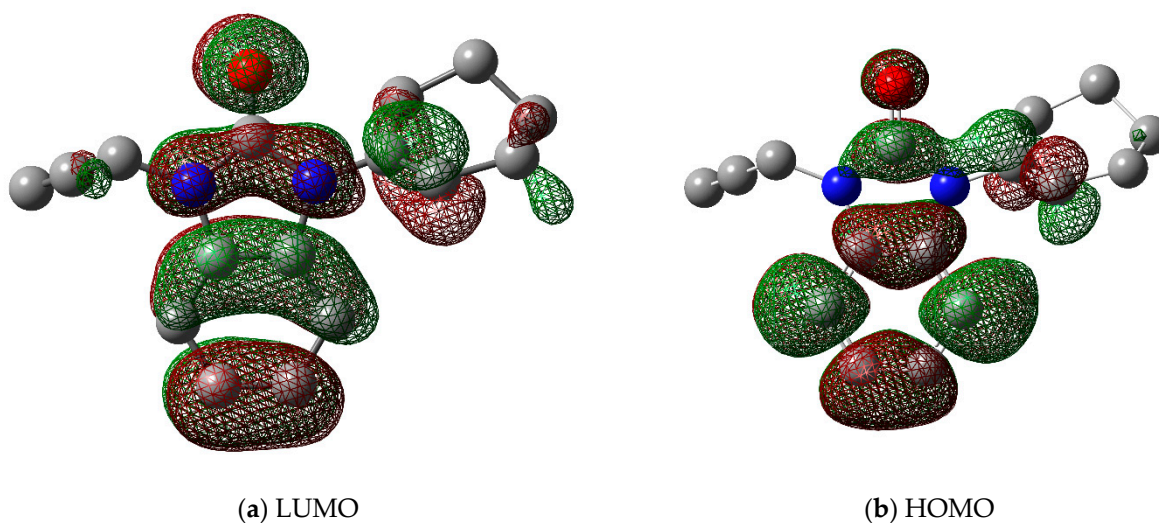
**Figure 5.** Stacking of layers along the *a*-axis direction. Hydrogen atoms are omitted for clarity.

The measured X-ray data and the computed geometry parameters, including bond lengths and bond angles, are listed in Table 4. The ORTEP, optimized geometry, and superimposition of the X-ray structure alongside the optimized structure are shown in Figure 2. After aligning the optimized ideal molecular geometry obtained through DFT calculations with the final geometry of **2** derived from the X-ray data, the determination of the root mean square deviation (RMSD) value becomes feasible through superposition, as shown in Figure 3c. This process allows a quantitative assessment of the structural congruence between the experimentally determined X-ray structure and the theoretically optimized molecular geometry. From the alignment (Figure 3c), it is clear the optimized geometry is superimposed upon the experimental one with an overlay similarity of 0.98%, which means that the puckering potential is consistent at the B3LYP level, except for the cyclohexenyl ring that showed a small deviation. This deviation was confirmed by an RMSD value of 0.18. According to this, the DFT calculation yields a meaningful geometry of the benzimidazole-2-one (**2**), and the findings of the obtained experimental data from the X-ray correctly described the calculated geometric parameters. The findings revealed minimal heterogeneity between experimental and computational methods. From these results presented in Table 4 and depicted in Figure 2, the selected theoretical method and the basis set (i.e., B3LYP/6-311++G(d,p)) could be suitable for the DFT calculation study of (**2**).

A molecule with a large gap ( $\Delta E$ ) (i.e., the highest occupied molecular orbital (HOMO) minus the lowest unoccupied molecular orbital (LUMO)) has generally a high kinetic stability and a low chemical reactivity (Figure 6) [28]. In terms of the energetic stability of a molecule, it is unfavorable to add electrons to a high-lying HOMO and to remove electrons from a low-lying LUMO. Table 5 shows the calculated molecular reactivity parameters for the title molecule, including electronegativity ( $\chi$ ), ionization potential (IP), chemical potential ( $\mu$ ), chemical hardness ( $\eta$ ), chemical softness (*S*), and electron affinity index (EA).

**Table 4.** Selected geometrical parameters for the title compound 2.

Bond Lengths (Å), Bond Angles (°)	Experimental	Calculated DFT/B3LYP/6-311++G(d,p)
O1-C1	1.2237 (14)	1.222
N1-C1	1.3849 (16)	1.401
N1-C2	1.3956 (15)	1.402
N1-C8	1.4362 (16)	1.431
N2-C1	1.3806 (15)	1.396
N2-C7	1.3910 (15)	1.391
N2-C14	1.4541 (15)	1.431
C1-N1-C2	109.85 (10)	109.59
C1-N1-C8	123.81 (10)	123.50
C2-N1-C8	125.88 (10)	126.90
C1-N2-C7	110.49 (10)	110.51
C1-N2-C14	122.77 (10)	121.66
C7-N2-C14	126.69 (10)	127.77
O-C1-N1	126.89 (11)	127.96
O-C1-N2	127.09 (11)	126.30
N2-C1-N1	106.01 (9)	105.72
C3-C2-N1	131.39 (11)	131.85
N1-C2-C7	107.04 (10)	107.25
N2-C7-C2	106.61 (10)	106.90
C6-C7-N2	131.76 (11)	131.55
C9-C8-N1	119.37 (11)	120.07
N1-C8-C13	116.57 (12)	116.09
N2-C14-C15	111.65 (10)	113.76

**Figure 6.** Frontier molecular orbitals (a) LUMO and (b) HOMO of the title crystal 2.**Table 5.** Calculated chemical reactivity parameters for 2.

Descriptors	
$E_{\text{HOMO}}$	−5.8779 eV
$E_{\text{LUMO}}$	−0.6057 eV
Energy gap ( $\Delta E$ )	5.2722 eV
Ionization potential (I)	5.8779 eV
Electron affinity (EA)	0.6057 eV
Electronegativity ( $\chi$ )	2.6361 eV
Chemical hardness ( $\eta$ )	3.2418 eV



#### 2.4. Hirshfeld Surface Analysis

In view of visualizing the different intermolecular contacts in the crystal packing of compound **2**, an analysis using the Hirshfeld surface (HS) was performed. This method facilitates the identification of regions of interaction between pairs of atoms, shedding light on the contributions of these contacts. The analysis specifically highlights atoms with the potential to engage in hydrogen bonds and  $\pi$ -stacking interactions, providing valuable information on the nature and strength of intermolecular forces [29–31]. This approach improves our understanding of the spatial distribution and importance of specific atomic interactions within the crystal lattice. The  $d_{\text{norm}}$  (normalized contact distance) plays a crucial role in identifying the key sites for intermolecular contacts. In the context of the HS represented in  $d_{\text{norm}}$  (Figure 7), the white surface signifies the points which contact the van der Waals radii at intervals equidistant from their cumulative total. The distances of the van der Waals radius that are shorter (near touch) or longer (different contact) are represented by red and blue colors [30].

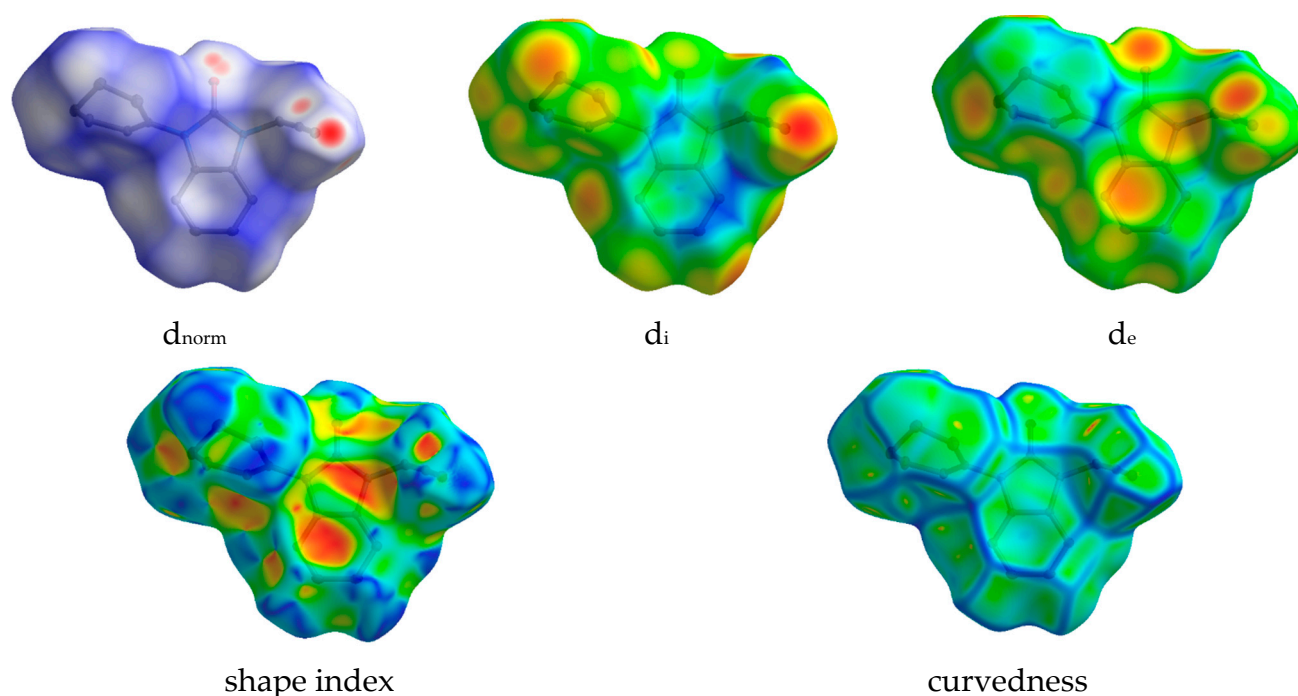


**Figure 7.** Hirshfeld surface mapped with  $d_{\text{norm}}$ ,  $d_i$ ,  $d_e$ , shape index, and curvedness for compound (**2**).

The  $d_{\text{norm}}$ ,  $d_i$ ,  $d_e$ , curvedness, and shape index are  $-0.2600$  to  $1.1859$ ,  $0.9684$  to  $2.4213$ ,  $0.9696$  to  $2.4592$  Å,  $-4$  to  $4$  and  $-1$  to  $1$ , respectively. The  $d_{\text{norm}}$ ,  $d_i$ ,  $d_e$ , shape index, and curvedness contour maps on a molecule HS are depicted in Figure 7. The analysis of  $\pi$ -stacking interactions is further aided by the HS shape index and curvedness plots, which are computed based on local curvatures. The presence of blue and green colors illustrates the packed stacking of a compound throughout the curvature. The 2D fingerprint plots quantified the contribution of each type of interaction to the HS. Red spots on the surface designate intermediate interactions taking into account the hydrogen bonds and the interatomic contacts between the molecules. As can be seen on the  $d_{\text{norm}}$  surface (Figure 7), the C-H $\cdots$ O intermolecular hydrogen bonds and C-H $\cdots$ Cg over the surface were indicated by the adjacent red–blue spots.

Dominant interactions within the HS are corroborated by the fingerprint diagrams, as illustrated in Figure 8, where one molecule acts as an acceptor ( $d_i > d_e$ ) while the other functions as a donor ( $d_e > d_i$ ). The 2D fingerprint diagrams, depicted in Figure 8, highlighted the prevalence of specific intermolecular contacts, with H $\cdots$ H and C $\cdots$ H interactions being

the most prevalent in **2**, constituting 56.3% and 25.5% of the total area, respectively. Other dominant forces are O $\cdots$ H/H $\cdots$ O (9.4%) and N $\cdots$ H/H $\cdots$ N (2.3%) contacts for (**2**). The presence of  $\pi$ - $\pi$ -stacking-type interactions in the shape index is corroborated by the flat green surface, delimited by a blue hump close to the red hollows, as well as a blue outline on the curvedness surface. The 2D fingerprint plots and the molecular HS regions are useful in clarifying the contributions of the different inter-contacts that participate in the stabilization of the crystal structure. These contributions indicate that the arrangement of **2** is predominantly influenced by the robust electrostatic interactions that drive the crystal-packing force in **2**.

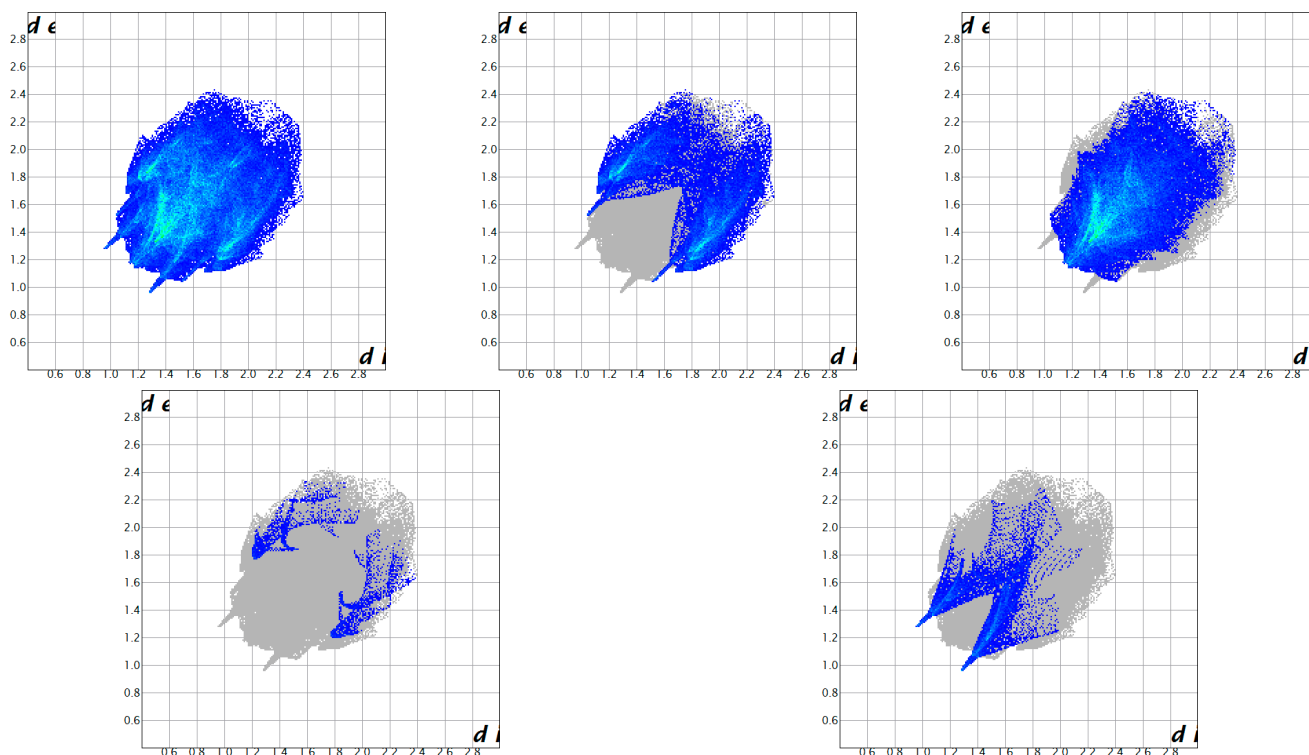


**Figure 8.** Two-dimensional fingerprint plots for **2**.

### 2.5. Molecular Electrostatic Potential (MEP)

The MEP is associated with the electronic density and serves as a valuable descriptor for identifying regions pertinent to nucleophilic and electrophilic reactions. It also aids in understanding chemical reactivity and hydrogen bonding interactions [32]. The various electrostatic potential values are visually represented with distinct colors: green represents zero potential regions, red represents the most negative electrostatic potential surface, and blue represents the most positive electrostatic potential areas. Within the MEP, the positive electrostatic potential (depicted by the blue areas) corresponds to the push exerted by nuclei, while the negative electrostatic potential (represented by yellow and red) is associated with the electrostatic charge of a proton and the overall electron density within the molecule. The negative electrostatic potential (shown by the yellow and red regions) is largely located on the nitrogen and oxygen atoms, making them the most reactive places for an electrophilic assault, as seen in Figure 9. In contrast, hydrogen atoms have a positive electrostatic potential (indicated by the blue patches), indicating that they are the most reactive places for a nucleophilic attack.

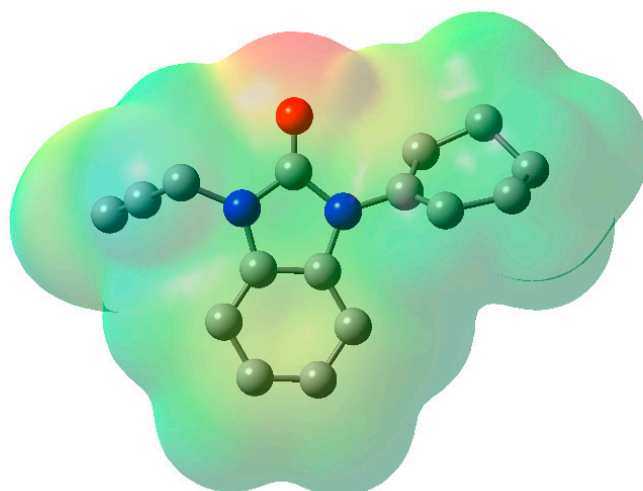


**Figure 9.** Molecular electrostatic potential map of **2**, Hydrogen atoms were omitted for clarity.

### 2.6. Pharmacological Analysis

To determine the bioactivity of benzimidazolone (**2**), the physicochemical and pharmacokinetic properties were examined using the SwissADME web tool, and the results are shown in Table 6. Compound (**2**) meets the topological polar surface area (TPSA) criteria specified by the Egan rule ( $TPSA \leq 132 \text{ \AA}^2$ ) and the Veber rule ( $TPSA \leq 140 \text{ \AA}^2$ ) [33,34]. The LogP values aid in determining the transport and binding behavior of medicinal molecules inside the body [35]. The SwissADME tool predicts LogP values using five different models, and the average of the five predicted LogP values represents the lipophilicity of our produced molecule. Molecule (**2**) has a high absorption rate in the gastrointestinal (GI) tract. The negative log Kp value indicates that title chemical (**2**) is less skin-permeant [36].

**Table 6.** Drug-like properties of **2** estimated through the use of SwissADME online tool.

Drug-Like Parameter	Benzimidazolone ( <b>2</b> )
Formula	C <sub>16</sub> H <sub>16</sub> N <sub>2</sub> O
Molecular weight (g/mol)	252.31 g/mol
H-bond acceptors	1
H-bond donors	0
Rotatable bonds	2
TPSA (Å <sup>2</sup> )	26.93 Å <sup>2</sup>
iLOGP	3.03
GI absorption	High
log Kp (cm/s)	−5.94 cm/s
Lipinski violations	Yes *
Veber violations	Yes *
Egan violations	Yes *
Muegge violations	Yes *
Bioavailability score	0.55

\*: No violation.

The toxicity of molecule (**2**) was calculated using the GUSAR online tool and is illustrated in Table 7. According to these results, title molecule (**2**) belongs to the toxic (Class 4) group in the oral mode and the slightly harmful (Class 4) group in the intraperitoneal (IP) and subcutaneous (SC) modes.

**Table 7.** Estimated acute toxicity prediction for molecule (2) using the GUSAR server.

LD <sub>50</sub>	LD50 (mg/kg)
Rat Intraperitoneal (IP)	317.3 #
Rat Intravenous route (IV)	29.02 *
Rat Oral	1181.00 #
Rat Subcutaneous route (SC)	411.80 #

\* Molecule in Class 4; # Molecule in Class 3.

### 3. Experimental and Computational Methods

#### 3.1. General

The determination of melting points was carried out using an open capillary Buchi 510 instrument. The spectroscopic analysis, involving <sup>13</sup>C NMR (75 MHz) and <sup>1</sup>H NMR (300 MHz), was conducted on a Bruker spectrometer. The recorded spectra present numerical values of chemical shifts in parts per million (ppm), relative to tetramethylsilane (TMS) set as the reference at 0.00 ppm. This methodology ensures precision and accuracy in assessing both the physical and spectroscopic characteristics of the compounds under investigation. A Triple TOFTM 5600 LC/MS-MS System (AB SCIEX) was utilized to acquire high resolution mass spectral data. The ion spray voltage, in the 5500 ionization mode, was utilized in the mass spectra. To perform column chromatography, E-Merck silica gel 60-F254 was used. To monitor the progression of the reaction, thin-layer chromatography (TLC) was employed, utilizing silica gel 60-F254. The UV-light method was employed for spot detection at a wavelength of 254 nm. Standard purification procedures were applied to purify reagents and solvents before their use in the experiment, ensuring the reliability and accuracy of the analytical results. A EuroEA Elemental Analyser was utilized to measure the elemental analysis of 2.

#### 3.2. Synthesis of Alkylated Benzimidazolones (2)

A mixture of 1-(cyclohex-1-en-1-yl)-1,3-dihydro-2H-benzimidazol-2-one (1) (4.7 mmol), benzyltriethylammonium chloride (2.3 mmol), and potassium carbonate (14.69 mmol) in a mixture of *N,N*-dimethylformamide and acetonitrile (15 mL, 3:2 *v/v*) was heated at 90 °C for 30 min. After cooling, propargyl bromide (4.8 mmol) was added. The mixture was stirred at room temperature for 6 h. The reaction mixture was diluted with 30 mL of distilled water and then extracted three times with 30 mL of dichloromethane. Anhydrous sodium sulfate was used to dry the mixed organic layers. The solvent was evaporated under vacuum, and the residue was purified using column chromatography on silica gel using a hexane/ethyl acetate mixture (8/2) as eluent. This procedure made it possible to obtain a pure and isolated product with a yield of 85% [22].

Characterization of 1-(Cyclohex-1-en-1-yl)-3-(prop-2-yn-1-yl)-1,3-dihydro-2H-benzimidazol-2-one (2)

White solid. Yield: 85%, 0.95 g, m.p. 118–120 °C (ethyl acetate). IR (KBr,  $\nu$  (cm<sup>-1</sup>), 2125 (C≡CH), 1710 (2C=O). <sup>1</sup>H NMR (CDCl<sub>3</sub>):  $\delta$ ppm: 1.63, 1.73, 2.16, 2.40 (4m, 8H, 4CH<sub>2</sub>-cyclohex-1-enyl), 2.15 (t, *J* = 3 Hz, 1H, HC≡C), 4.56 (d, *J* = 3 Hz, 2H, N-CH<sub>2</sub>-C), 5.82 (m, 1H, HC=C-, H- cyclohex-1-enyl), 6.89–7.14 (m, 4H, H-Ar). <sup>13</sup>C NMR (CDCl<sub>3</sub>):  $\delta$ ppm: 21.63, 22.56, 24.71, 26.75 (4C, 4CH<sub>2</sub>, C- cyclohex-1-enyl), 30.37 (1C, N-CH<sub>2</sub>-C), 72.67 (1C, HC≡C), 127.41 (4C, =CH-, C-Ar), 128.56, 129.67, 132.15 (4C, =C-, C-quaternary), 154.60 (1C, C=O). HRMS of [M+H]<sup>+</sup> *m/z* 253.1335, calcd for C<sub>16</sub>H<sub>17</sub>N<sub>2</sub>O, found: 253.1296. *Anal.* Calcd for C<sub>16</sub>H<sub>16</sub>N<sub>2</sub>O: C, 76.16; H, 6.39; N, 11.10. Found: C, 76.56; H, 6.27; N, 11.22.

#### 3.3. Crystal Structure Determination and Refinement

The benzimidazolone (2) was selected and X-ray intensity data were collected at 296 K on a Bruker APEX-II QUAZAR CCD graphite-monochromated Mo-K $\alpha$  radiation ( $\lambda$  = 0.71073 Å). A complete data set was processed using Bruker SAINT. The structure solution was obtained via direct methods using SHELXT [37] and refined through a full

matrix, least-squares on  $F^2$  using SHELXL [37]. The cyclohexenyl ring is disordered over two sites in a 0.844(3)/0.156(3) ratio. The two moieties were resolved and refined with some restraints that their geometries be comparable. The crystallographic characteristics, details of X-ray data collection and structure refinement parameters for 1-(cyclohexenyl)-3-(prop-2-ynyl)-1,3-dihydro-2H-benzimidazol-2-one (**2**) are listed in Table 2. The H atoms bound to carbon were placed in calculated positions with C-H = 0.93–0.97 Å and refined in the riding-model approximation with Uiso (H) = 1.5 Ueq of the parent atom. The residual electron density in the final difference Fourier map was between  $-0.23 < Dq < 0.75$ . The geometry of the title crystal molecule **2** was resolved and refined using WinGX [38], SHELXL, and Mercury [39].

### 3.4. DFT Calculations

The molecular structure was optimized and the harmonic vibrational frequencies of compound **2** were computed using the same DFT/B3LYP on a 6-311G++(d,p) basis set using the Gaussian program 09W without any restrictions on geometry. The obtained vibrational frequencies of the optimized compound using the B3LYP/6-311++G(d,p) in the gas phase were scaled by 0.9627 [40].

Hirshfeld surface (HS) analysis was carried out to determine the type of intermolecular contacts. The 2D fingerprint plots and molecular surface regions for **2** were created to offer information about the percentage contribution as well as the major and minor intermolecular contributors. The HS was mapped using  $d_{\text{norm}}$ , the shape index, curvature, and 2D fingerprint plots generated using Crystal Explorer 17 [41]. The primary goal of quantum chemistry lies in elucidating the molecular geometry, chemical reactivity, energy, and the intricacies of chemical bonds. DFT calculations were employed in this study to gain insights into the electrophilic and nucleophilic structures. The current investigation consists of structural and chemical properties and spectroscopic details, as well as both local indicators (molecular electrostatic potential (MEP)) and global descriptors like softness and hardness parameters. These assessments were conducted using the DFT/B3LYP/6-311++G(d,p) method, providing a comprehensive understanding of the molecular behavior and reactivity.

### 3.5. Drug-Likeness Prediction

The drug-like physicochemical and pharmacokinetic properties of the synthesized compound were estimated using the SwissADME online server [42]. The acute toxicity of the title molecule **2** was estimated using the GUSAR (General Unrestricted Structure-Activity Relationships) web tool by calculating the LD<sub>50</sub> values for oral, intravenous (IV), intraperitoneal (IP), and subcutaneous (SC) administration methods [43].

## 4. Conclusions

Benzimidazolone (**2**) was prepared via the liquid-solid phase-transfer alkylation method from benzimidazolone (**1**). The structure of the alkylated benzimidazolone was characterized via <sup>1</sup>H-NMR, <sup>13</sup>C-NMR, HRMS, and X-ray analysis. This research aimed to explore the various hydrogen-bonding modes and  $\pi$ - $\pi$  interactions in the solid. The Hirshfeld surface analysis assisted in identifying and understanding these intermolecular interactions. The 2D fingerprint plots revealed that H...H and C...H/H...C intermolecular interactions are the most important contributors to these interactions.

**Supplementary Materials:** The following supporting information can be downloaded at: <https://www.mdpi.com/article/10.3390/cryst13121661/s1>. <sup>1</sup>H-NMR, <sup>13</sup>C-NMR and HRMS spectra of **2** can be found in the Supplementary Materials.

**Author Contributions:** Conceptualization, M.A. and I.H.; methodology, M.L., D.C. and A.B.; software, M.A., M.A.L. and I.H.; validation, M.A.L., M.M.A., D.C. and A.B.; formal analysis, M.A., H.M., S.F. and M.F.; investigation, M.A., I.H. and M.M.A.; data curation, M.A. and I.H.; writing original draft preparation, M.A. and I.H.; visualization, M.A.L., I.H.; M.M.A. and A.B.; supervision, D.C. and A.B. All authors have read and agreed to the published version of the manuscript.

**Funding:** This research was supported by the Researchers Supporting Project number (RSPD2023R628), King Saud University, Riyadh, Saudi Arabia.

**Institutional Review Board Statement:** Not applicable.

**Informed Consent Statement:** Not applicable.

**Data Availability Statement:** The crystallographic data for the structure reported in this article have been deposited at the Cambridge Crystallographic Data Center, under deposition number CCDC 2176903. A copy of the data can be obtained free of charge from <https://www.ccdc.cam.ac.uk/structures/> (accessed on 10 October 2023). All other relevant data generated and analyzed during this study, including experimental, spectroscopic, crystallographic, and computational data, are included in this article and its Supplementary Information.

**Acknowledgments:** The authors would like to thank Joel T. Mague at the X-ray Crystallography Laboratory (School of Science and Engineering, Tulane University, USA) for his assistance with the final refinement of the molecule.

**Conflicts of Interest:** The authors declare no conflict of interest.

## References

1. Zhang, S.-L.; Damu, G.L.V.; Zhang, L.; Geng, R.-X.; Zhou, C.-H. Synthesis and Biological Evaluation of Novel Benzimidazole Derivatives and Their Binding Behavior with Bovine Serum Albumin. *Eur. J. Med. Chem.* **2012**, *55*, 164–175. [[CrossRef](#)]
2. Alpan, A.S.; Parlar, S.; Carlino, L.; Tarikogullari, A.H.; Alptüzün, V.; Güneş, H.S. Synthesis, Biological Activity and Molecular Modeling Studies on 1H-Benzimidazole Derivatives as Acetylcholinesterase Inhibitors. *Bioorg. Med. Chem.* **2013**, *21*, 4928–4937. [[CrossRef](#)] [[PubMed](#)]
3. Hernández-Luis, F.; Hernández-Campos, A.; Castillo, R.; Navarrete-Vázquez, G.; Soria-Arteche, O.; Hernández-Hernández, M.; Yépez-Mulia, L. Synthesis and Biological Activity of 2-(Trifluoromethyl)-1H-Benzimidazole Derivatives against Some Protozoa and *Trichinella Spiralis*. *Eur. J. Med. Chem.* **2010**, *45*, 3135–3141. [[CrossRef](#)] [[PubMed](#)]
4. Mulugeta, E.; Samuel, Y. Synthesis of Benzimidazole-Sulfonyl Derivatives and Their Biological Activities. *Biochem. Res. Int.* **2022**, *2022*, 7255299. [[CrossRef](#)]
5. Refaat, H.M. Synthesis and Anticancer Activity of Some Novel 2-Substituted Benzimidazole Derivatives. *Eur. J. Med. Chem.* **2010**, *45*, 2949–2956. [[CrossRef](#)] [[PubMed](#)]
6. Chandrika, N.T.; Shrestha, S.K.; Ngo, H.X.; Garneau-Tsodikova, S. Synthesis and Investigation of Novel Benzimidazole Derivatives as Antifungal Agents. *Bioorg. Med. Chem.* **2016**, *24*, 3680–3686. [[CrossRef](#)] [[PubMed](#)]
7. Starčević, K.; Kralj, M.; Ester, K.; Sabol, I.; Grce, M.; Pavelić, K.; Karminski-Zamola, G. Synthesis, Antiviral and Antitumor Activity of 2-Substituted-5-Amidino-Benzimidazoles. *Bioorg. Med. Chem.* **2007**, *15*, 4419–4426. [[CrossRef](#)] [[PubMed](#)]
8. Tonelli, M.; Simone, M.; Tasso, B.; Novelli, F.; Boido, V.; Sparatore, F.; Paglietti, G.; Pricl, S.; Giliberti, G.; Blois, S.; et al. Antiviral Activity of Benzimidazole Derivatives. II. Antiviral Activity of 2-Phenylbenzimidazole Derivatives. *Bioorg. Med. Chem.* **2010**, *18*, 2937–2953. [[CrossRef](#)]
9. Patagar, D.N.; Batakurki, S.R.; Kusanur, R.; Patra, S.M.; Saravanakumar, S.; Ghate, M. Synthesis, Antioxidant and Anti-Diabetic Potential of Novel Benzimidazole Substituted Coumarin-3-Carboxamides. *J. Mol. Struct.* **2023**, *1274*, 134589. [[CrossRef](#)]
10. Acar Çevik, U.; Celik, I.; Paşayeva, L.; Fatullayev, H.; Bostancı, H.E.; Özkay, Y.; Kaplancıklı, Z.A. New Benzimidazole-oxadiazole Derivatives: Synthesis,  $\alpha$ -glucosidase,  $\alpha$ -amylase Activity, and Molecular Modeling Studies as Potential Antidiabetic Agents. *Arch. Der Pharm.* **2023**, *356*, 2200663. [[CrossRef](#)]
11. Singh, N.; Pandurangan, A.; Rana, K.; Anand, P.; Ahamad, A.; Tiwari, A.K. Benzimidazole: A Short Review of Their Antimicrobial Activities. *Int. Curr. Pharm. J.* **2012**, *1*, 110–118. [[CrossRef](#)]
12. El-Gohary, N.S.; Shaaban, M.I. Synthesis and Biological Evaluation of a New Series of Benzimidazole Derivatives as Antimicrobial, Antiquorum-Sensing and Antitumor Agents. *Eur. J. Med. Chem.* **2017**, *131*, 255–262. [[CrossRef](#)]
13. Chen, G.; Liu, Z.; Zhang, Y.; Shan, X.; Jiang, L.; Zhao, Y.; He, W.; Feng, Z.; Yang, S.; Liang, G. Synthesis and Anti-Inflammatory Evaluation of Novel Benzimidazole and Imidazopyridine Derivatives. *ACS Med. Chem. Lett.* **2013**, *4*, 69–74. [[CrossRef](#)] [[PubMed](#)]
14. Yoon, Y.K.; Ali, M.A.; Wei, A.C.; Choon, T.S.; Osman, H.; Parang, K.; Shirazi, A.N. Synthesis and Evaluation of Novel Benzimidazole Derivatives as Sirtuin Inhibitors with Antitumor Activities. *Bioorg. Med. Chem.* **2014**, *22*, 703–710. [[CrossRef](#)] [[PubMed](#)]
15. Obot, I.B.; Obi-Egbedi, N.O. Theoretical Study of Benzimidazole and Its Derivatives and Their Potential Activity as Corrosion Inhibitors. *Corros. Sci.* **2010**, *52*, 657–660. [[CrossRef](#)]

16. Adardour, M.; Lasri, M.; Ait Lahcen, M.; Maatallah, M.; Idouhli, R.; Alanazi, M.M.; Lahmidi, S.; Abouelfida, A.; Mague, J.T.; Baouid, A. Exploring the Efficacy of Benzimidazolone Derivative as Corrosion Inhibitors for Copper in a 3.5 Wt.% NaCl Solution: A Comprehensive Experimental and Theoretical Investigation. *Molecules* **2023**, *28*, 6948. [[CrossRef](#)]
17. Rossi, A.; Hunger, A.; Kebrle, J.; Hoffmann, K. Benzimidazol-Derivate und verwandte Heterocyklen V. Die Kondensation von o-Phenylendiamin mit aliphatischen und alicyclischen  $\beta$ -Ketoestern. *Helv. Chim. Acta* **1960**, *43*, 1298–1313. [[CrossRef](#)]
18. Adardour, M.; Zaballos-García, E.; Loughzail, M.; Dahaoui, S.; Baouid, A. Synthesis, Characterization and X-Ray Structure of Heterocyclic Systems Prepared via 1,3-Dipolar Cycloaddition of Nitrile Oxides with Benzimidazolone. *J. Mol. Struct.* **2018**, *1165*, 153–161. [[CrossRef](#)]
19. Nath, J.; Paul, R.; Ghosh, S.K.; Paul, J.; Singha, B.; Debnath, N. Drug Repurposing and Relabeling for Cancer Therapy: Emerging Benzimidazole Antihelminthics with Potent Anticancer Effects. *Life Sci.* **2020**, *258*, 118189. [[CrossRef](#)]
20. Elhenaw, A.; Al-Wasidi, A.; Refat, M.; Naglah, A. Different Potential Biological Activities of Benzimidazole Derivatives. *Egypt. J. Chem.* **2021**, *64*, 3–5. [[CrossRef](#)]
21. Hernández-López, H.; Tejada-Rodríguez, C.J.; Leyva-Ramos, S. A Panoramic Review of Benzimidazole Derivatives and Their Potential Biological Activity. *Mini Rev. Med. Chem.* **2022**, *22*, 1268–1280. [[CrossRef](#)] [[PubMed](#)]
22. Adardour, M.; Boutafda, A.; Hdoufane, I.; Aghraz, A.; Hafidi, M.; Zaballos-García, E.; Cherqaoui, D.; Baouid, A. Efficient and Simple Synthesis of Novel 1,2,3-Triazolyl-Linked Benzimidazolone, Molecular Docking and Evaluation of Their Antimicrobial Activity. *Synth. Commun.* **2020**, *50*, 3490–3506. [[CrossRef](#)]
23. Saber, A.; Sebbar, N.K.; Sert, Y.; Alzaqri, N.; Hökelek, T.; El Ghayati, L.; Talbaoui, A.; Mague, J.T.; Baba, Y.F.; Urrutigoity, M.; et al. Syntheses of N-Substituted Benzimidazolone Derivatives: DFT Calculations, Hirshfeld Surface Analysis, Molecular Docking Studies and Antibacterial Activities. *J. Mol. Struct.* **2020**, *1200*, 127174. [[CrossRef](#)]
24. Veena, K.; Raghu, M.S.; Yogesh Kumar, K.; Pradeep Kumar, C.B.; Alharti, F.A.; Prashanth, M.K.; Jeon, B.-H. Design and Synthesis of Novel Benzimidazole Linked Thiazole Derivatives as Promising Inhibitors of Drug-Resistant Tuberculosis. *J. Mol. Struct.* **2022**, *1269*, 133822. [[CrossRef](#)]
25. Saber, A.; Anouar, E.H.; Sebbar, G.; Ibrahim, B.E.; Srhir, M.; Hökelek, T.; Mague, J.T.; Ghayati, L.E.; Sebbar, N.K.; Essassi, E.M. New 1,2,3-Triazole Containing Benzimidazolone Derivatives: Syntheses, Crystal Structures, Spectroscopic Characterizations, Hirshfeld Surface Analyses, DFT Calculations, Anti-Corrosion Property Anticipation, and Antibacterial Activities. *J. Mol. Struct.* **2021**, *1242*, 130719. [[CrossRef](#)]
26. Othman, D.I.A.; Hamdi, A.; Tawfik, S.S.; Elgazar, A.A.; Mostafa, A.S. Identification of New Benzimidazole-Triazole Hybrids as Anticancer Agents: Multi-Target Recognition, in Vitro and in Silico Studies. *J. Enzym. Inhib. Med. Chem.* **2023**, *38*, 2166037. [[CrossRef](#)] [[PubMed](#)]
27. Cremer, D.; Pople, J.A. General Definition of Ring Puckering Coordinates. *J. Am. Chem. Soc.* **1975**, *97*, 1354–1358. [[CrossRef](#)]
28. Yang, P.; Zhu, Z.; Chen, M.; Zhou, X.; Chen, W. Microwave-Assisted Synthesis of Polyamine-Functionalized Carbon Dots from Xylan and Their Use for the Detection of Tannic Acid. *Spectrochim. Acta Part A Mol. Biomol. Spectrosc.* **2019**, *213*, 301–308. [[CrossRef](#)]
29. Hirshfeld, F.L. Bonded-Atom Fragments for Describing Molecular Charge Densities. *Theoret. Chim. Acta* **1977**, *44*, 129–138. [[CrossRef](#)]
30. Spackman, M.A.; McKinnon, J.J.; Jayatilaka, D. Electrostatic Potentials Mapped on Hirshfeld Surfaces Provide Direct Insight into Intermolecular Interactions in Crystals. *CrystEngComm* **2008**, *10*, 377–388. [[CrossRef](#)]
31. Spackman, M.A.; Jayatilaka, D. Hirshfeld Surface Analysis. *CrystEngComm* **2009**, *11*, 19–32. [[CrossRef](#)]
32. Louroubi, A.; Nayad, A.; Hasnaoui, A.; Hdoufane, I.; Idouhli, R.; Saadi, M.; El Ammari, L.; Abdessalam, A.; Berraho, M.; El Firdoussi, L.; et al. Synthesis, Structural Characterization, Theoretical Studies and Corrosion Inhibition of a New Pyrrole Derivative: 1-(1-Benzyl-4-(4-Chlorophenyl)-2,5-Dimethyl-1H-Pyrrol-3-yl)ethanone. *J. Mol. Struct.* **2019**, *1189*, 240–248. [[CrossRef](#)]
33. Veber, D.F.; Johnson, S.R.; Cheng, H.-Y.; Smith, B.R.; Ward, K.W.; Kopple, K.D. Molecular Properties That Influence the Oral Bioavailability of Drug Candidates. *J. Med. Chem.* **2002**, *45*, 2615–2623. [[CrossRef](#)]
34. Egan, W.J.; Merz, K.M.; Baldwin, J.J. Prediction of Drug Absorption Using Multivariate Statistics. *J. Med. Chem.* **2000**, *43*, 3867–3877. [[CrossRef](#)] [[PubMed](#)]
35. Rutkowska, E.; Pajak, K.; Józwiak, K. Lipophilicity—Methods of Determination and Its Role in Medicinal Chemistry. *Acta Pol. Pharm.* **2013**, *70*, 3–18. [[PubMed](#)]
36. Chen, C.-P.; Chen, C.-C.; Huang, C.-W.; Chang, Y.-C. Evaluating Molecular Properties Involved in Transport of Small Molecules in Stratum Corneum: A Quantitative Structure-Activity Relationship for Skin Permeability. *Molecules* **2018**, *23*, 911. [[CrossRef](#)]
37. Sheldrick, G.M. SHELXT—Integrated Space-Group and Crystal-Structure Determination. *Acta Crystallogr. Sect. A Found. Crystallogr.* **2015**, *71*, 3–8. [[CrossRef](#)]
38. Farrugia, L. WinGX and ORTEP for Windows: An Update. *J. Appl. Crystallogr.* **2012**, *45*, 849–854. [[CrossRef](#)]
39. Macrae, C.F.; Edgington, P.R.; McCabe, P.; Pidcock, E.; Shields, G.P.; Taylor, R.; Towler, M.; Van De Streek, J. Mercury: Visualization and Analysis of Crystal Structures. *J. Appl. Crystallogr.* **2006**, *39*, 453–457. [[CrossRef](#)]
40. Andersson, M.P.; Uvdal, P. New Scale Factors for Harmonic Vibrational Frequencies Using the B3LYP Density Functional Method with the Triple- $\zeta$  Basis Set 6-311+G(d,p). *J. Phys. Chem. A* **2005**, *109*, 2937–2941. [[CrossRef](#)]

41. Spackman, P.R.; Turner, M.J.; McKinnon, J.J.; Wolff, S.K.; Grimwood, D.J.; Jayatilaka, D.; Spackman, M.A. *CrystalExplorer: A program for Hirshfeld surface analysis, visualization and quantitative analysis of molecular crystals*. *J. Appl. Cryst.* **2021**, *54*, 1006–1011. [[CrossRef](#)] [[PubMed](#)]
42. Daina, A.; Michielin, O.; Zoete, V. SwissADME: A Free Web Tool to Evaluate Pharmacokinetics, Drug-Likeness and Medicinal Chemistry Friendliness of Small Molecules. *Sci. Rep.* **2017**, *7*, 42717. [[CrossRef](#)] [[PubMed](#)]
43. Lagunin, A.; Zakharov, A.; Filimonov, D.; Poroikov, V. QSAR Modelling of Rat Acute Toxicity on the Basis of PASS Prediction. *Mol. Inf.* **2011**, *30*, 241–250. [[CrossRef](#)] [[PubMed](#)]

**Disclaimer/Publisher’s Note:** The statements, opinions and data contained in all publications are solely those of the individual author(s) and contributor(s) and not of MDPI and/or the editor(s). MDPI and/or the editor(s) disclaim responsibility for any injury to people or property resulting from any ideas, methods, instructions or products referred to in the content.